Eur. Phys. J. D **4**, 231–238 (1998)

THE EUROPEAN PHYSICAL JOURNAL D

Laser applications for atmospheric pollution monitoring

E. Frejafon[1], J. Kasparian[1], P. Rambaldi[1], B. Vezin[1], V. Boutou[1], J. Yu[1], M. Ulbricht[2], D. Weidauer[2], B. Ottobrini[3], E. de Saeger[3], B. Krämer[4], T. Leisner[4], P. Rairoux[4], L. Wöste[4], and J.P. Wolf[1]

[1] LASIM[a], Université Claude Bernard Lyon I, 43 boulevard du 11 novembre 1918, 69622 Villeurbanne Cedex, France
[2] Elight Laser Systems GmbH Warthestrasse 21, 14513 Teltow/Berlin, Germany
[3] ERLAP, Joint Research Center, via E. Fermi, 21020 Ispra, Italy
[4] Institut für Experimentalphysik, Freie Universität Berlin, Arnimallee 14, 14195 Berlin, Germany

Received: 18 February 1998 / Revised: 2 April 1998 / Accepted: 15 April 1998

Abstract. In this paper, we present an overview of the capabilities of linear and non-linear spectroscopy for the 3D-analysis of gaseous pollutants and aerosols in the atmosphere. The basic technique is Lidar (Light Detection and Ranging). Results obtained in Sevilla and Lyon about the ozone smog formation and the dynamics of the transport of dust particles are presented. Finally, non-linear Mie scattering on atmospheric aerosols has been demonstrated in the laboratory, opening new perspectives for remote sensing.

PACS. 42.68.-w Atmospheric optics – 42.62.Fi Laser spectroscopy – 92.60.Sz Air quality and air pollution

1 Introduction

Recent advances of tunable all solid state laser systems and in the Lidar technique (Light Detection and Ranging) opened new perspectives in the 3D-analysis of atmospheric pollution dynamics.

3D mappings of concentrations of pollutants such as NO, NO_2, SO_2, O_3 and Toluene have been obtained, allowing a direct access to the physical and chemical dynamics of air pollution [1]. The major part of the studies were dedicated to urban conditions, in the frame of large scale measurement campaigns in European cities (Lyon, Stuttgart, Leipzig, Geneva, Berlin, Zürich, Athens). These campaigns put into evidence the importance of topography and micrometeorology, such as street canyon turbulence [1–3].

In the present paper, recent results giving a detailed description of the photochemistry of tropospheric ozone production are presented, which were obtained during summer smog episodes in Sevilla (Spain). The spatial and temporal dynamics of the ozone generation through traffic emission and transport are observed in the city, and also in the surrounding areas up to 20 km far from Sevilla centre.

Besides detection of gaseous pollutant, Lidar allows to a certain extent the detection of urban aerosols, and in particular of dust particles. However, due to the complexity of the problem (size distribution, shape and composition of the mixture of aerosols), these measurements were often limited to qualitative information (backscatter profiles) [4].

We present here a novel method, combining scanning electronic microscopy (SEM), X-Ray Microanalysis, and Lidar data. This combined technique allowed us to obtain the first quantitative 3D profiles of aerosols concentration in urban conditions in Lyon. The basis of the method is a newly developed fractal model to invert the Lidar data.

Finally, in order to increase the number of observables using Lidar, we performed laboratory experiments evaluating the feasibility of a femtosecond non-linear Lidar system. These first experiments were very encouraging, since backscattering in non-linear Mie scattering is much more important than in the linear angular dependency.

2 The Lidar technique

When a laser beam is sent into the atmosphere, it is widely scattered in every direction by particles present in the air. This scattering is essentially caused by Rayleigh scattering on Nitrogen and Oxygen molecules, and Mie scattering on aerosols (dusts, water droplets, ...). In a Lidar arrangement, the backscattered light is collected by a telescope, usually placed coaxially with the laser emitter (see Fig. 1). The signal is then focused onto a photodetector through a spectral filter, adapted to the laser wavelength. Since a pulsed laser is used, the intensity of the backscattered light can be recorded as a function of time, and then provide spatial resolution. The received signal reflects the aerosol and molecular concentration *versus* range. More precisely, the received number of photons $M(R, \lambda)$ from a distance R at a wavelength λ (assuming that each photon is

[a] UMR 5579

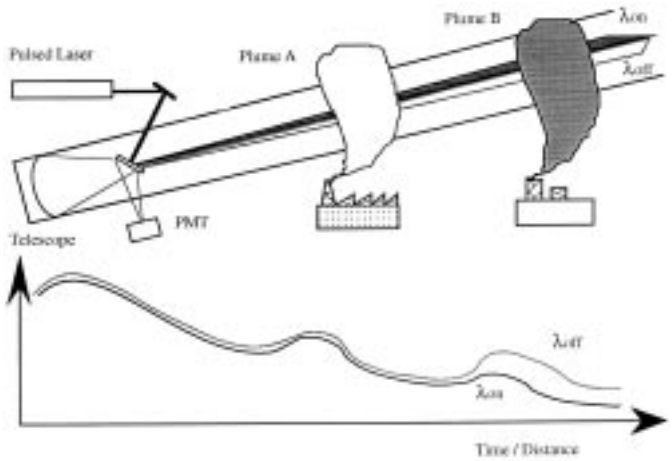

Fig. 1. Lidar and DIAL principles.

scattered only once) is given by [4]:

$$M(R,\lambda) = M_0(\lambda)\frac{A_0}{R^2}\beta(R,\lambda)\Delta R\xi(R,\lambda) \times \exp\left[-2\int_0^R \alpha(R,\lambda)dR\right] \quad (1)$$

where: $M_0(\lambda)$ is the number of photons emitted by the laser, A_0 is the area of the telescope, ΔR is the spatial resolution of the system, essentially limited by the laser pulse duration t, $\Delta R = ct/2$, $\beta(R,\lambda)$ is the volume backscattering coefficient, $\xi(R,\lambda)$ is the detection efficiency, and $\alpha(R,\lambda)$ is the total atmospheric extinction coefficient.

The detection efficiency $\xi(R,\lambda)$ takes into account every geometrical and optical factors of the receiver arrangement. $\xi(R,\lambda)$ can be separated in two different parameters, one dedicated to the spectral characteristics $\xi(\lambda)$ of the detection channels (filters, monochromator, ...), and the other, $\xi(R)$, to geometrical properties such as the overlap between the field illuminated by the laser and the telescope field of view. This latter parameter is often used to somewhat compress the large dynamic range of the signal.

The signal dependence on the aerosol concentration, which allows their detection, is included in two scattering parameters: the volume backscattering coefficient β and the extinction α. However, the exponential factor $\exp\{-2\int\alpha(R,\lambda)dR\}$ represents the total atmospheric attenuation of the laser beam *via* the Beer-Lambert law. The extinction is caused by two different processes: the Rayleigh-Mie scattering α_{RM} and the specific absorption coefficient α_A of the different molecules present in the atmosphere. The α_{RM} extinction coefficient, like β, is an average over every size, shape and composition of the aerosols. To invert equation (1), a usual method is to use a reduced form with a fitted α_{RM}/β ratio (see Sect. 4 and [14]).

The α_A allows a specific detection of a particular gaseous pollutant, using the Differential Absorption Lidar (DIAL) technique.

The DIAL technique is based on the use of a pair of wavelengths close to each other, with a large absorption coefficient difference (called λ_{on} and λ_{off}, for on-resonance and off-resonance wavelength respectively).

Let us now assume that such a pair of wavelengths (λ_{on}, λ_{off}) selected for a pollutant "B", is sent simultaneously into the atmosphere (Fig. 1). Since λ_{on} and λ_{off} have been chosen close enough for exhibiting the same scattering properties, the first plume A of Figure 1 (which does not contain the detected species "B") causes an increase of the backscattered signal, because the concentration of aerosols is larger than in the clear atmosphere, but the same increase for both pulses. Conversely, the second chimney plume, which contains a certain amount of the pollutant, will absorb the backscattered signal at the λ_{on}-wavelength much stronger than at the λ_{off}-one. From this difference, and using Beer-Lambert's law, one obtains the specific concentration of the pollutant considered as a function of distance. More precisely, if we take the ratio of the two Lidar returns (represented each by Eq. (1)), and take the derivative of its logarithm, we have that:

$$N_A(R) = \frac{1}{2(\sigma(\lambda_{on}) - \sigma(\lambda_{off}))}\frac{d}{dR}\ln\left(\frac{M(R,\lambda_{off})}{M(R,\lambda_{on})}\right) \quad (2)$$

where $N_A(R)$ is the pollutant number density, and $\sigma(\lambda)$ the absorption cross-section at the wavelength λ.

The concentration of the species is then measured range resolved and, by scanning the field of investigation in azimuth or elevation, 2D or 3D mappings are obtained, like a molecule-specific Radar.

From an experimental point of view, all the Lidar/DIAL results presented here were obtained using "all solid state" Lidar systems. They are based on our previously described high energy dual-wavelength flashlamp pumped Ti:Sapphire laser (Elight Laser Systems, 300 mJ/20 Hz), frequency doubled or tripled. The implementation goes from very compact laboratory systems until mobile, van transported, fully automatic devices. These systems have been extensively described before [1], and the latest version is marketed by Elight Laser Systems. Typical specifications of such Lidar systems are in Table 1 where ΔK is the differential absorption coefficient and is related to the absorption cross-sections by $\Delta K = (\sigma(\lambda_{on}) - \sigma(\lambda_{off}))\, N_{STP}$. N_{STP} is the atmospheric molecular number density at standard temperature and pressure: 2.56×10^{19} cm^{-3}. It allows to express the pollutants concentration values in parts per million (ppm) or parts per billion (ppb), which is usual in atmospheric chemistry, instead of molecules/cm^3.

3 Three-dimensional measurements of gaseous pollutants: ozone in Sevilla

As an example of three-dimensional measurements of gaseous pollution, we present here the results of an ozone measurement campaign in Sevilla during June 96.

Ozone is one of the most important pollutant responsible for the summer "smog" recorded in large urban areas.

Table 1. Typical specifications of Lidar systems.

Pollutant	λ_{on} (nm)	λ_{off} (nm)	ΔK (1/cm atm)	Energy (mJ)	Sensitivity (ppb)	Range (km)
SO_2	286.55	285.7	10.2	5	8	3
O_3	283.0	287.0	27.4	5	4	3
NO	226.80	226.83	105	1	2	1
NO_2	398.29	397.5	4.5	25	15	4
Toluene	266.9	266.1	29.5	7	7	3
Benzene	258.9	257.9	38.7	7	5	3

Its formation is particularly due to the emission of road traffic (Nitrogen Oxides, Volatile Organic Compounds) combined with important sunny periods. Photolysis is the dominant loss process for NO_2 in the troposphere and is the major source of tropospheric O_3 [22]:

$$NO_2 + h\nu \rightarrow NO + O(^3P) \quad (3)$$

$$O(^3P) + O_2 + M \rightarrow O_3 + M \quad (4)$$

where M is a third body.

Since NO is oxidized back to NO_2,

$$O_3 + NO \rightarrow O_2 + NO_2 \quad (5)$$

$$RO_2 + NO \rightarrow RO + NO_2 \quad (6)$$

it is established a "photostationary cycle", in which the ozone concentration is determined by the solar flux (reaction (3)) and the VOC/NO_x ratio (the mainly VOC reactive radicals R being alkyl or acyl compounds). More precisely:

$$[O_3] = \frac{\frac{j_3[NO_2]}{[NO]} - k_6[RO_2]}{k_5} \quad (7)$$

where j_3 is the photolysis constant of reaction 3, k_5 is the second order rate constant for reaction (5) and k_6 is a generalized second order rate constant for the reactions with peroxyradicals.

The measurements in Sevilla have been mainly performed at three particularly representative sites. The first series of mappings is recorded in the town centre. Profiles are carried out along a road with a very important traffic, interrupted with many traffic lights. The results presented in Figure 2a, show an average concentration of about 50 ppb with peaks, up to 80 ppb on the beginning of the afternoon when solar radiation is at its maximum. During the night, the concentration stabilizes around 35 ppb, although it remains very important at altitudes around 200 m. Without the solar photodissociation of NO_2, oxidation of nitrogen monoxide takes place and yields lower ozone concentration. At ground level, the depletion of ozone is further enhanced by the titration of O_3 by NO emitted by traffic and by deposition. As very usually observed [22], the VOC/NO_x in the centre of large cities is too low to obtain maximum ozone production.

Nevertheless, it has to be noticed that because of the reduction of convection processes during night time, ozone survives at higher altitude.

The second series of measurements has been performed in a rural area, upwind from Sevilla during the measurements: La Riconada (results are presented in Fig. 2b). The concentrations were usually low, from 35 ppb during the night to 50 ppb in the day time, close to the ozone background level. This is well-understood, since the Sevilla city plume is propagating in the opposite direction and thus almost no nitrogen oxides (as well as O_3) is imported. The population is weakly exposed unlike the population in the centre of Sevilla.

The third site chosen for the Lidar measurements was downwind from Sevilla (San Lucar) during the measurement period, 22 km far from the city, in a totally rural zone. This region is well-known for its agricultural production. Long distance transport of the Sevilla nitrogen oxides encounters then local biogenical (isoprene, terpene) production of VOC's, which yields very favorable VOC/NO_x ratios for ozone production [22]. Moreover, part of the ozone coming from Sevilla is transported as well. The results are interesting (Fig. 2c) since quite high ozone concentrations are observed, relatively homogeneous in space and time: 50 ppb in average with peaks at 70 ppb. These concentrations are still important during the night owing to the fact that the local road traffic (and thus NO) is low.

The results presented here precisely show on the one hand the influence of the meteorological conditions on the ozone formation, and on the other hand the importance of transport processes of urban pollution. The effect of the aerosols concentration on the ozone production is, however, not taken into account, and even not fully understood yet. Quantitative measurements of aerosols by Lidar are thus an important challenge, as described below.

4 Quantitative analysis of urban aerosols

The impacts of atmospheric aerosols on public health and in heterogeneous chemistry are well-recognized although few definitely concluding studies were reported so far. This is especially true for urban aerosols, the variety of which in size and composition makes a complete characterization difficult. In this paper, we present a combined technique, using Lidar measurements, scanning electronic microscopy (SEM) and X-Ray microanalysis.

Urban aerosols are first sampled using standard techniques on different filters. Their size is determined by SEM and counting and their composition by X-ray microanalysis. These data are then used to compute backscattering

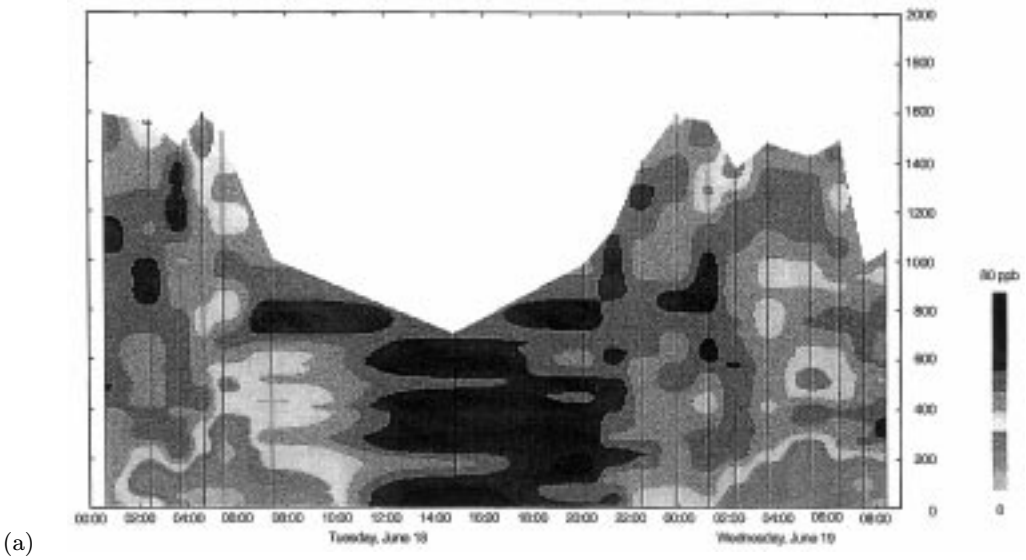

(a)

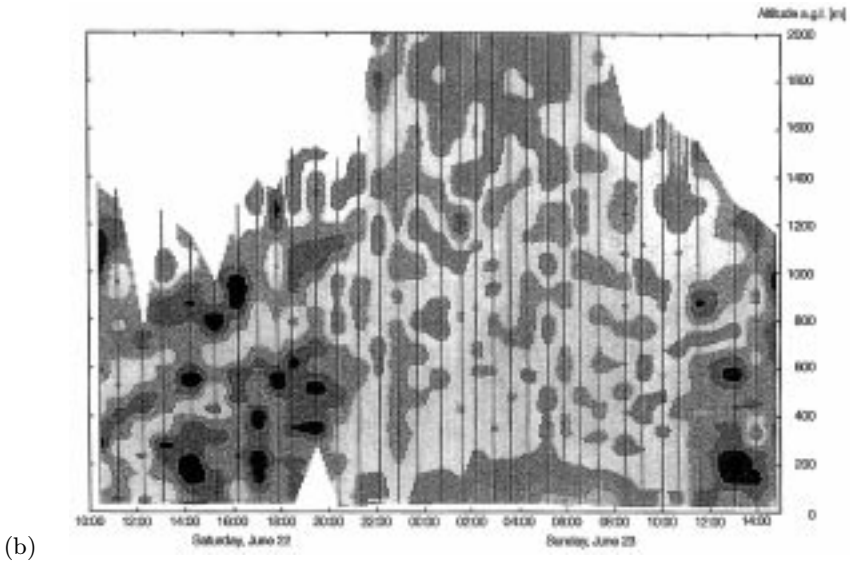

(b)

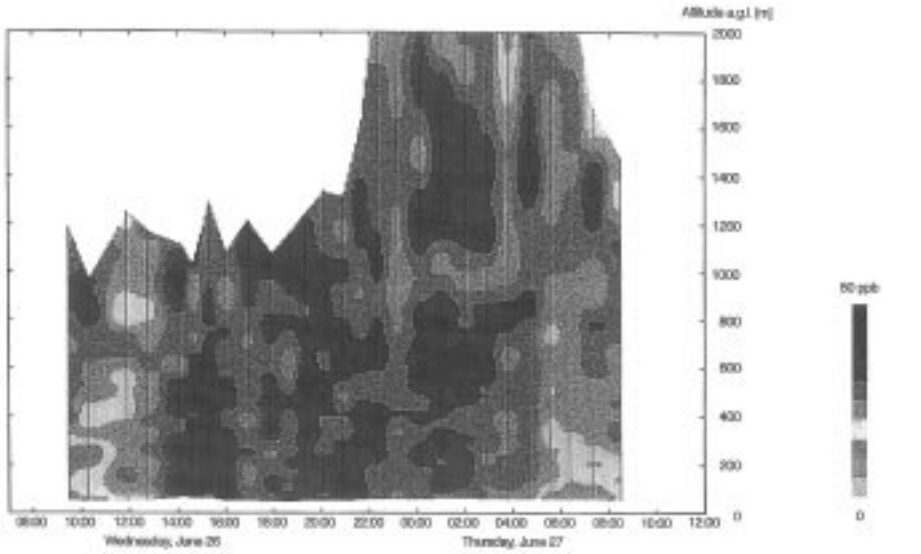

(c)

Fig. 2. Results of the ozone campaign in Sevilla. (a) Sevilla centre; (b) Upwind from Sevilla; (c) 22 km downwind from the city.

Fig. 3. Typical SEM image of impacted urban aerosols.

and extinction coefficients, leaving as the only unknown parameter the total density of particles. The number density profiles over Lyon are obtained by simultaneous Lidar measurements using an eye-safe Lidar system. The Lidar data are inverted with the backscattering and extinction coefficients computed using a newly developed fractal algorithm from the actual size distribution. These measurements have been performed in the frame of an intensive campaign between June 15 and September 15, 1996.

Typical SEM image of the filters is presented in Figure 3. Three main species of particles are identified. The most common type is composed of very small (around 0.1 μm) particles, which agglomerate in rough aggregates with dimensions up to 3 μm. The second type is made of bigger (1 μm), smooth particles. Crystalline particles also appear, but their number density on the filters is much lower.

The three aerosol families that can be distinguished on SEM images have also different X-ray signatures.The most abundant particles, the smaller ones, exhibit high peaks of carbon and sulphur elements. These are characteristic of soot aerosols produced by Diesel car engines, with sulphur compounds adsorbed on them. The smooth particles, mainly exhibit silicon and oxygen, that is typical of silica. The result corresponding to the crystalline particles mainly show the silicon, calcium, potassium, sodium and iron elements. These suggest the composition of feldspath and black mica. This is also consistent with their aspect. We therefore assign them as granitic dust due to erosion.

The knowledge of the backscattering and extinction coefficients α_{RM} and β is necessary to invert the Lidar data. In this section, we show a novel method for determining these coefficients based on the information extracted from SEM imaging and X-ray microanalysis. The latter technique gives the composition of the particles encountered in the atmosphere. We therefore can infer their index of refraction and compute their individual α and β coefficients as a function of size.

Soot particles in the smaller mode originate from combustion, their shape therefore exhibits a fractal character [5,6]. Due to the high absorption of soot particles, we can consider their extinction and absorption coefficients to be almost equal. If we denote their fractal dimension as D, their gyration radius as R_g and the number of monomers by aggregate as N, their absorption and scattering cross-sections can be expressed as [7,8]:

$$\sigma_{abs}^{fractal} = -4Nk\pi a^3 \mathrm{Im}\left(\frac{m^2-1}{m^2+2}\right) \tag{8}$$

$$\frac{d\sigma_{diff}^{aggregate}(\theta)}{d\Omega} = N^2 S(x) k^4 a^6 \left|\frac{m^2-1}{m^2+2}\right|^2 \tag{9}$$

where m is the refractive index of the monomers and a is their radius supposed small compared with the wavelength, k is the wavenumber and S is a structure factor [9]:

$$S(x) = \left(1 + \frac{2x^2}{3D}\right)^{-\frac{D}{2}} \tag{10}$$

where

$$x = qR_g = \frac{4\pi}{\lambda} R_g \sin\left(\frac{\theta}{2}\right) \cdot \tag{11}$$

For the bigger mode, soot particles appear much too compact on the SEM images to be described with a fractal growth. In their formation, they encounter collisions and rearrangements of the monomers. Moreover, the overall shape on of the aggregates is more or less of spherical symmetry. We therefore describe them as a sphere composed of mixed soot and void [14]. If we denote ϕ the soot volume fraction, their effective complex refractive index can be approximated in the visible domain by [14,15]:

$$m = (1+\phi) + \phi i. \tag{12}$$

In our case, we estimate the volume fraction to be about 50%. As for silica particles (refractive index $m = 1.486 + 0i$), they are assumed as spheres. Extinction and backscattering efficiencies are computed from the Mie theory. Both types exhibit a rather smooth dependence of the extinction efficiency with the particle size. In the opposite, the results for backscattering are quite different from one another. In the case of silica, the result exhibits many sharp resonances due to morphology dependent resonances [16,17]. Those resonances are smoothed down in the case of soot particles since the high imaginary part of their refractive index destroys the high-Q modes responsible for the resonances.

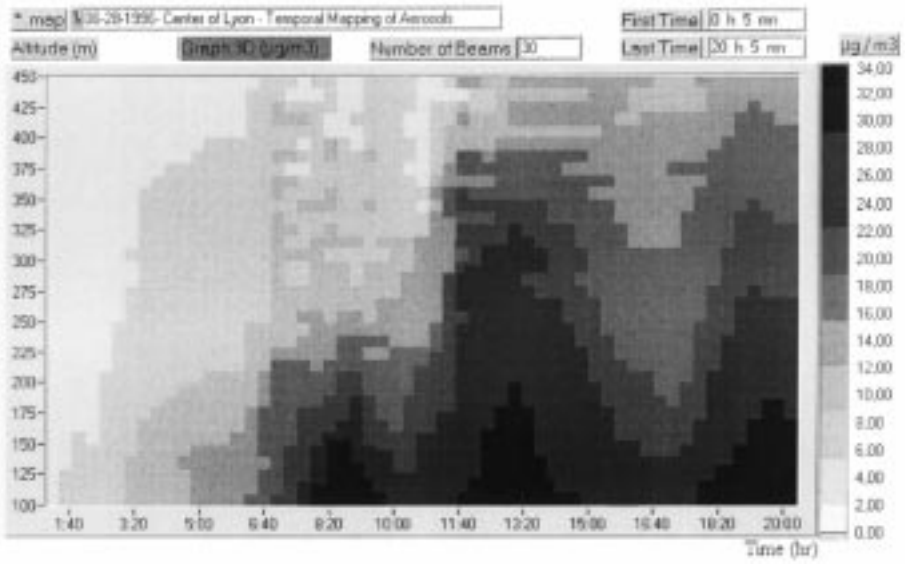

Fig. 4. Temporal evolution of the aerosols concentration over Lyon.

Due to their rarity, granitic particles are not taken into account and as the relative humidity was very low during the measurements, water droplets are also neglected. Given the extinction and backscattering efficiencies for individual particles, it is easy to determine the size dependence of these efficiencies for the size range observed on the filters. We then combine this information with the size distribution. This gives out a global α/β value of $43sr$. This value enables now to run the Lidar inversion algorithm.

Lidar measurements have been performed from the roof of a building located in the north of the city of Lyon. To fulfill eye safety requirements, all measurements were made at 390 nm. Data were inverted using a Klett algorithm [14] with 2 reference points: one located close from ground with the α and β values determined in the previous paragraph, and one at high altitude where a clear atmosphere is assumed. In the conditions encountered here, the assumption of an average size distribution is acceptable (warm stable afternoon).

Quantitative 3D-distributions of aerosols over the city have been monitored. The results show a pretty homogeneous mixing layer up to 1300 m. An interesting measurement is also the temporal behavior of the concentrations of these urban aerosols. Figure 4 shows the temporal evolution of the vertical profile of aerosol concentration in Lyon over 24 hour during a high-pollution episode, on June 27-28, 1996. It shows very clearly the motion of the mixing layer height. Due to the temperature changes, it goes down to 200 m during night and explodes up in the early morning. Traffic aerosols cause also a clear increase in aerosol density during rush hours, in the morning around 8 a.m., at noon, and in the evening around 6 p.m. Concentration as high as 40 μg/m^3 are observed during these rush hours.

5 Non linear scattering of light by microdroplets

In this last section, we emphasize the fact that a precise knowledge of the aerosols size distribution is required to achieve reliable quantitative information from the Lidar equation inversion. Unfortunately, classical methods (like impaction and counting of particles) used to characterize the aerosol load in the air are bound with large constraints (see Sect. 4). It is therefore relevant to develop other methods to analyze particles. The tentative strategy adopted here is to take advantage of the fact that quality factors Q of microdroplets can be very high, due to their small size and spherical shape [15]. The idea is appealing since this high Q property enhances non-linear optical effects. We present first results about the angular dependence of non-linear (third harmonic) Mie scattering.

The experimental setup is described in details elsewhere [16]. Briefly, monodisperse water droplets are generated at a repetition rate of 1 kHz by a piezo-driven nozzle. Depending on the operation conditions of the nozzle, droplets in the size range between 8 and 32 μm could be produced. The microdroplets beam intersect the synchronized beam of a Ti:Sa femtosecond laser which produces ultrafast light pulses (80 fs) with pulse energies of 400 μJ at a central wavelength of 820 nm. The scattered light is collected with a quartz fiber, spectrally analyzed in a UV spectrometer and finally detected by a photomultiplier tube. The quartz fiber is mounted onto a stepper motor driven goniometer in order to detect the scattered light emitted by the illuminated particles at various angles between 18 and 180° and with an angular resolution of almost 1°.

The spectral dependence of non linear scattering from water microdroplets with a typical radius of 25 μm has been recorded. A typical spectrum is given in Figure 5. The main feature is a prominent THG (third harmonic

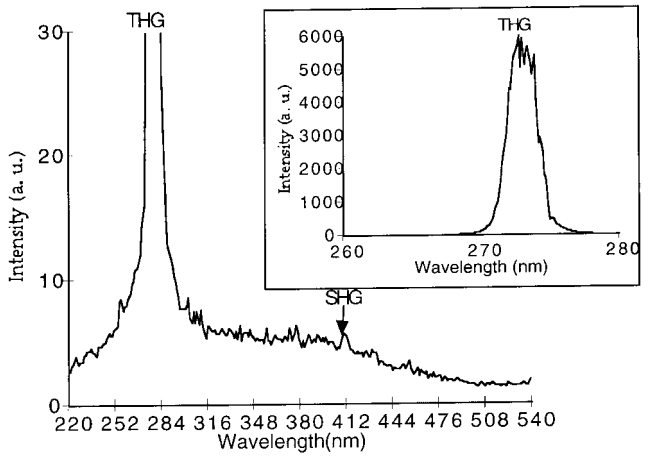

Fig. 5. Non-linear scattered spectrum from a 25 μm micro-droplet.

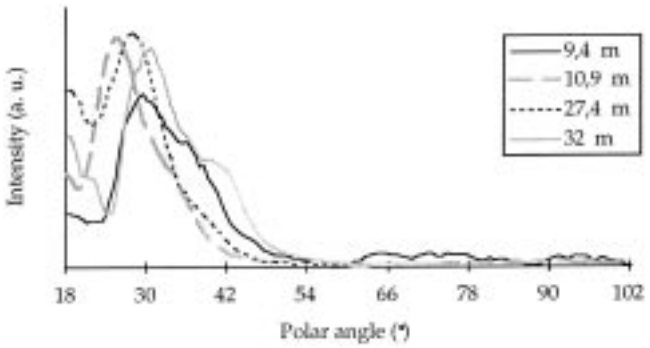

Fig. 6. Angular dependence of the THG emission from micro-droplets.

generation) peak centered at 273 nm. As expected, the THG overall intensity at low laser power is proportional to the third power of the intensity at the fundamental frequency coupled into the droplet. The other non linear processes, for example the second harmonic generation (SHG) or the white light emission process are several orders of magnitude weaker than the THG. In particular, the SHG peak at 410 nm is rather weak. This is indeed an indication of the good spherical shape of the water droplets since SHG is forbidden by symmetry in the case of perfectly spherical particles. Moreover, no stimulated Raman scattering was observed in contrast with other experiments conducted by Chang *et al.* in the picosecond regime [17]. Nevertheless, this is understandable with respect to the short laser pulses used, shorter than the typical build-up time required for the Raman scattering process [18,19]. These observations demonstrate that THG is indeed the dominant non linear channel.

The THG angular dependence is given in Figure 6 for detection angles ranging from 18 to 102°. It has been recorded for various sizes of the water droplet between 9.4 and 32 μm. For each size, we notice a steep maximum near the forward scattering direction (28). An intense maximum is also detected for backward scattering angles near 150°. Moreover, the intensity of the light scattered near the forward and backward directions are of the same order of magnitude for the THG non linear process. Such a pattern strongly contrasts with that of the linear case. Linear Mie computations completely fail to reproduce the experimental results. However, computations based on a non linear extension of the linear Mie theory have also been undertaken [16,20,21]: a fair agreement between measurements and the extended non linear Mie theory is achieved over the measurement range.

The pattern of the THG distribution observed for droplets of 10.5 μm radius remains remarkably stable for the whole size range (from 8 to 32 μm). In comparison to linear Mie scattering which leads to numerous scattering maxima at various angles, highly correlated to the size of the particle, the pattern is always simple and does not change much for particle size in that range. However, a breakdown of this stable situation might happen for smaller size particles. To get some insight into the THG for smaller particles (around 1 μm), we have studied the cloud produced by the droplets exploding under high power laser illumination [21]: it appears that for sub-micron particles, the stabilization effect vanishes.

Finally, of particular interest might be femtosecond Lidar measurements. In order to explore a possible use of a femtosecond Lidar for droplets measurements, we have recorded the THG backscattered light in our experimental arrangements. To compare with linear Mie theory scattering processes, an effective back-scattered cross-section has been extracted from our measurements [21]. This value is only 4 orders of magnitude lower than in the case of linear Mie scattering. This observation is likely to open interesting future prospect in femtosecond Lidar.

6 Conclusion

Laser spectroscopy methods offer very promising methods of analyzing air pollution. The most attractive feature is their capability of providing 3D-range resolved measurements of concentrations of gaseous and solid particles. A further novel aspect, which seems to make the technique even more attractive is to use non-linear laser spectroscopy. Besides the example presented here, very recent experiments demonstrated the use of it in a white light Lidar experiment using high energy femtosecond lasers [23].

References

1. D. Weidauer, P. Rairoux, M. Ulbricht, J.P. Wolf, L. Wöste, in *Advances in Atmospheric Remote Sensing with Lidar*, edited by A. Ansmann, R. Neuber, P. Rairoux, U. Wandinger (Springer Verlag, 1996), p. 423.
2. H.J. Kölsch, P. Rairoux, J.P. Wolf, L. Wöste L., Appl. Phys. B **54**, 89 (1992).
3. H.J. Kölsch, P. Rairoux, D. Weidauer, J.P. Wolf, L. Wöste, J. Phys. III France **4**, 643 (1994).
4. R.M. Measures, *Laser Remote Sensing* (Wiley, New York, 1984).

5. S. Gangopadadhyay, I. Elminawi, C. Sorensen, Appl. Opt. **30**, 4859 (1991).
6. C. Sorensen, J. Cai, N. Lu, Appl. Opt. **31**, 6547 (1992).
7. M.V. Berry, I.C. Percival, Optica Acta **33**, 577 (1986).
8. T. Freltoft, J.K. Kjems, S.K. Sinha, Phys. Rev. B **33**, 269 (1986).
9. G. Dietler, C. Aubert, D.S. Cannell, P. Wiltzius, Phys. Rev. Lett. **57**, 3117 (1986).
10. P. Chylek, V. Ramaswamy, R. Cheng, R.G. Pinnick, Appl. Opt. **20**, 2980 (1981).
11. S.C. Graham, Combust. Sci. Technol. **9**, 159 (1974).
12. V. Lefevre-Seguin, J.C. Knight, V. Saandoghar, D.S. Weiss, J. Hare, J.-M. Raimond, S. Haroche, *Advances in Applied Physics*, edited by R.K. Chang, A.J. Campillo, Vol. 3 (1997).
13. J.D. Eversole, H.-B. Lin, A.L. Huston, A.J. Campillo, P.T. Leung, S.Y. Liu, K. Young, J. Opt. Soc. Am. **10**, 1955 (1993).
14. J.D. Klett, Appl. Opt. **24**, 1638 (1985).
15. J.-Z. Zhang, D.H. Leach, R.K. Chang, Opt. Lett. **13**, 270 (1988).
16. J. Kasparian, B. Krämer, J.P. Dewitz, S. Vadja, P. Rairoux, B. Vezin, V. Boutou, T. Leisner, W. Hübner, J.-P. Wolf, L. Wöste, K.H. Bennemann, Phys. Rev. Lett. **78**, 2952 (1997).
17. D.H. Leach, R.K. Chang, W.P. Acker, S.C. Hill, J. Opt. Soc. Am. B **10**, 34 (1993).
18. M. Suzuki, K. Midorikawa, H. Tashiro, J. Opt. Soc. Am. B **8**, 1000 (1991).
19. M.D. Duncan, R. Mahon, L.L. Tankersley, J. Reintjes, J. Opt. Soc. Am. B **5**, 37 (1988).
20. J.P. Dewitz, W. Hübner, K.H. Bennemann, Z. Phys. D **37**, 75 (1996).
21. J. Kasparian, B. Krämer, T. Leisner, P. Rairoux, V. Boutou, B. Vezin, J.-P. Wolf, J. Opt. Soc. Am. B (1997) (submitted).
22. *Rethinking the Ozone Problem in Urban and Regional Air Pollution* (National Academy Press, Washington, 1992), 475 pages.
23. L. Wöste, C. Wedekind, H. Wille, P. Rairoux, B. Stein, S. Nikolov, C. Werner, S. Niedermeier, F. Ronneberger, H. Schillinger, R. Sauerbrey, Laser Optoelektr. **5**, 14 (1997).